

Three-Dimensional Eulerian–Eulerian Modeling of Gaseous Pollutant Emissions from Circulating Fluidized-Bed Combustors

Jun Xie,[†] Wenqi Zhong,^{*,†} Baosheng Jin,[†] Yingjuan Shao,[†] and Hao Liu[‡]

[†]Key Laboratory of Energy Thermal Conversion and Control of Ministry of Education, School of Energy and Environment, Southeast University, Nanjing, Jiangsu 210096, People's Republic of China

[‡]Energy and Sustainability Research Division, Faculty of Engineering, University of Nottingham, University Park, Nottingham NG7 2RD, United Kingdom

ABSTRACT: In this paper, a three-dimensional numerical model has been developed to study the gaseous pollutant emissions during the circulating fluidized-bed (CFB) combustion of combustible solid waste. On the basis of the Eulerian–Eulerian approach, the gas phase is modeled with a $k-\epsilon$ turbulent model and the particle phase is modeled with a kinetic theory of granular flow. The hydrodynamics, heat and mass transfer, and chemical reactions are simultaneously taken into account. Reactions during combustion consist of waste devolatilization, volatile combustion, char combustion, SO_2 formation and recapture by calcium oxide, NO and N_2O formation, and diminution by heterogeneous and homogeneous reactions. The model has been applied to the CFB riser with a height of 1.8 m and a diameter of 0.125 m at atmosphere. The influences of an excess air ratio on the emissions of SO_2 , NO, and N_2O are studied. The model predicts a growth in the SO_2 emission when excess air increases. The emissions of NO and N_2O also gradually increase with the increasing excess air ratio. Meanwhile, the CO and CH_4 concentrations show a decreasing tendency. The distribution of the bed voidage, flow pattern development, profiles of gas compositions, and related reaction rates inside the riser are also discussed.

1. INTRODUCTION

Nowadays, there is significant public awareness in relation to the hazard of gaseous pollutant emissions into the atmosphere from fuel combustion to obtain energy. Major pollutants in the flue gas consist of SO_2 , NO_x , N_2O , CO, and volatile organic compounds (HC). Sulfur and nitrogen contents in fuel can be oxidized to SO_2 and NO_x , respectively, which contribute to acid rain formation.¹ Carbon monoxide in general is the product of incomplete combustion of carbon-based compounds. The emission of nitrous oxide is not generally perceived to be a major problem but can be significant in a specific temperature range.² CO and N_2O are considered to be the greenhouse gas. The circulating fluidized-bed (CFB) combustion technology, which allows for clean and efficient combustion of various solid fuels, such as coal, biomass, and municipal solid waste (MSW), has received a lot of attention in recent years. Other advantages, such as the potential to reduce SO_2 and NO_x emissions, explain the increasing interest for this technology.³

Mathematical modeling of CFB combustion can improve the reactor design and save the operating cost arisen from the parametric studies.⁴ In the last 2 decades, various mathematical models have been developed to study gaseous pollutant emissions from coal, biomass, or waste combustion.^{5–12} However, most of the studies focus on the equilibrium model and kinetic model, which describe the fluid mechanics with empirical or semi-empirical correlations instead of solving the momentum equations. The computational fluid dynamics (CFD) model targets toward fundamental investigations of the fluid and chemical mechanical aspects of the fluidized bed.¹³

Modeling of fluid dynamics with the CFD method has progressed to reach a high present-day level, while CFD modeling of reactive multiphase flows is still in an early stage.¹⁴ There are

two kinds of multiphase CFD models: Eulerian–Eulerian model and Eulerian–Lagrangian model. In the Eulerian–Eulerian model, the solid phase is considered as a continuous phase interpenetrating and interacting with the gaseous phase. In the Eulerian–Lagrangian model, the trajectory and state (temperature, mass, composition, and velocity) of each individual particle are tracked in space and time by integrating the equations of mass, momentum, and energy for each particle in the system, but it is computationally expensive, especially if coupled with chemical reactions.¹³ Only a few papers have been found modeling gaseous pollutant emissions with multiphase CFD models. Rong and Horio¹⁵ developed a two-dimensional (2D) discrete element method (DEM)–CFD model to analyze the thermodynamic characteristics and NO emission of burning chars in a fluidized bed. The numbers of char particles and inert particles are 20 and 2000, respectively. NO emission is simplified to be formed with carbon combustion and reduced by carbon. Zhao et al.¹⁶ and Wang et al.¹⁷ presented Eulerian–Lagrangian models to predict the particle-clustering effects on SO_2 and NO emissions in CFB combustors. The clusters in the two models have 19 and 165 particles, respectively. These char particles are assumed to be stationary while combusting. Zhou et al.¹⁸ established an Eulerian–Eulerian model to investigate nitrogen and sulfur oxide emissions in a CFB combustor. In their work, the three-dimensional (3D) CFB riser was assumed as 2D. Yu et al.¹⁹ also applied the 2D two-fluid model to investigate SO_2 and NO_x emissions in the CFB combustor. It should be improved because the data derived from a 2D model

Received: May 14, 2014

Revised: July 25, 2014

Published: July 27, 2014

cannot be directly applied to the real 3D system considering the different effects of the bed walls and geometry on the flow pattern and other aspects.²⁰ Therefore, the 3D modeling is needed. Meanwhile, both Zhou et al.¹⁸ and Yu et al.¹⁹ validated the model by just one case. Various operating conditions and their influences on gaseous pollutant emission should be investigated.

The present work has developed a 3D Eulerian–Eulerian model to study the gaseous pollutant emission in a CFB waste combustor. The complex gas–solid flow, heat and mass transfer, and chemical reactions are simultaneously considered. Reactions during combustion consist of devolatilization, volatile combustion, char combustion, SO₂ recapturing, NO and N₂O formation, and reduction. The model is applied to the CFB riser with a height of 1.8 m and a diameter of 0.125 m at atmosphere. The influences of excess air ratio (EA) on the emissions of SO₂, NO, and N₂O are studied. The results are compared to experimental data. Simulations also obtain the formation and development of flow regimes, profiles of gas compositions, and related chemical rates inside the riser.

2. MODEL DESCRIPTIONS

On the basis of the Eulerian–Eulerian approach, the unsteady balance equations for mass, momentum, energy, and species are solved for gas and solid phases. The gas phase is modeled with the standard k – ε turbulence model. The constitutive relations for the solid phase are modeled using granular stress equations based on the kinetic theory of granular flow. The details of the model can be found in the literature.^{20,21} The governing equations are briefly presented as follows.

2.1. Governing Equations. The continuity equations for gas and solid phases are

$$\frac{\partial(\alpha_g \rho_g)}{\partial t} + \nabla(\alpha_g \rho_g \mathbf{v}_g) = S_{gs} \quad (1)$$

$$\frac{\partial(\alpha_s \rho_s)}{\partial t} + \nabla(\alpha_s \rho_s \mathbf{v}_s) = S_{gs} \quad (2)$$

where α , ρ , and \mathbf{v} represent the volume fraction, density, and gas velocity vector, respectively. S is the mass source term because of heterogeneous reactions, which is given by

$$S_{gs} = M_c \sum \gamma_r = -S_{sg} \quad (3)$$

where M , k , and r are the molecular weight, stoichiometric coefficient, and reaction rate, respectively.

The species conservation equations for species in the gas and solid phases can be written as

$$\frac{\partial(\alpha \rho Y_i)}{\partial t} + \nabla(\alpha \rho Y_i \mathbf{v}) = \nabla J_i + R_i \quad (4)$$

where Y_i is the mass fraction of species i , J_i is the diffusion flux, and R_i is the net rate.

$$J_i = -\left(\rho D_i + \frac{\mu_t}{Sc_t}\right) \nabla Y_i \quad (5)$$

where Sc_t is the Schmidt number and D is the turbulent mass diffusion coefficient.

The momentum equation for the gas phase can be written as

$$\begin{aligned} \frac{\partial(\alpha_g \rho_g \mathbf{v}_g)}{\partial t} + \nabla(\alpha_g \rho_g \mathbf{v}_g \mathbf{v}_g) \\ = -\alpha_g \nabla p + \alpha_g \rho_g \mathbf{g} - \beta(\mathbf{v}_g - \mathbf{v}_s) + \nabla(\alpha_g \tau_g) + S_{gs} \mathbf{v}_s \end{aligned} \quad (6)$$

where p is the gas pressure, τ_g is the gas stress tensor, β is the gas–solid interphase drag coefficient, and \mathbf{v}_s is the mean velocity of solid. The

Table 1. Proximate and Ultimate Analyses of Olive Cake

Proximate Analysis (wt %)	
fixed carbon	15.64
volatiles	68.82
ash	9.01
moisture	6.53
Ultimate Analysis (wt %, Dry Basis)	
C	46.80
H	6.07
O	36.69
N	0.68
S	0.12
ash	9.64
Ash Composition (wt %)	
CaO	32.38
Al ₂ O ₃	5.93
Fe ₂ O ₃	5.07
MnO ₂	1.41
Na ₂ O	49.82
SiO ₂	5.39

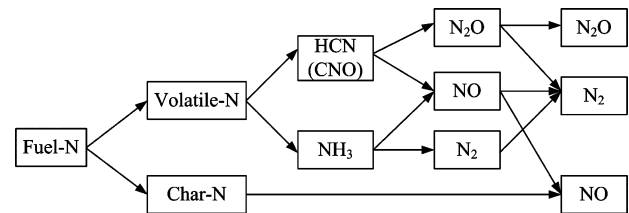


Figure 1. Fuel N conversion pathways.

term $S_{gs} \mathbf{v}_s$ is the momentum exchange between the gas and solid phases. The drag coefficient is based on the work by Syamlal and O'Brien²²

$$\beta = \frac{3}{4} \frac{\alpha_s \alpha_g \rho_l}{\nu_{ts}^2 d_s} C_D |\mathbf{v}_s - \mathbf{v}_g| \quad (7)$$

$$C_D = \left(0.63 + \frac{4.8}{\sqrt{Re_s / \nu_{ts}}} \right)^2 \quad (8)$$

where the ν_{ts} is the terminal velocity of solid.

$$\tau_g = \mu_g (\nabla \mathbf{v}_g + \nabla \mathbf{v}_g^T) - \frac{2}{3} \mu_g (\nabla \mathbf{v}_g) I \quad (9)$$

$$\mu_g = \mu_{gl} + \mu_{gt} \quad (10)$$

where μ_g is the gas shear viscosity, μ_{gl} is the laminar viscosity, and μ_{gt} is the turbulent viscosity, which is calculated from k and ε

$$\mu_{gt} = \rho_g C_\mu \frac{k^2}{\varepsilon} \quad (11)$$

where C_μ is a constant.

The governing transport equations for k and ε can be written as

$$\frac{\partial}{\partial t}(\alpha_g \rho_g k) + \nabla(\alpha_g \rho_g k \mathbf{v}_g) = \nabla \left(\alpha_g \frac{\mu_t}{\sigma_k} \nabla k \right) + \alpha_g G_k - \alpha_g \rho_g \varepsilon \quad (12)$$

$$\frac{\partial}{\partial t}(\alpha_g \rho_g \varepsilon) + \nabla(\alpha_g \rho_g \varepsilon \mathbf{v}_g) = \nabla \left(\alpha_g \frac{\mu_t}{\sigma_\varepsilon} \nabla \varepsilon \right) + \alpha_g \frac{\varepsilon}{k} (C_{\varepsilon 1} G_k - C_{\varepsilon 2} \rho_g \varepsilon) \quad (13)$$

where G_k is the generation of turbulence kinetic energy and defined as

$$G_k = \mu_{gt} \Delta \mathbf{v}_g \left[\Delta \mathbf{v}_g + (\Delta \mathbf{v}_g)^T - \frac{2}{3} \Delta \mathbf{v}_g (\mu_{gt} \Delta \mathbf{v}_g + \rho_g k) \right] \quad (14)$$

Table 2. Chemical Reaction Rates

	reaction rate r (kmol m ⁻³ s ⁻¹)	reaction rate constant K
R1	$r_1 = K_1 C_{\text{Oc}}$	$K_1 = 1.43 \times 10^3 \exp(-88600/RT)$
R2	$r_{2a} = K_2 C_{\text{CO}} C_{\text{O}_2}^{0.5}$	$K_2 = 1.0 \times 10^{15} \exp(-133024/RT)$
R3	$r_{3a} = K_3 C_{\text{H}_2}^{1.5} C_{\text{O}_2}$	$K_3 = 5.159 \times 10^{15} \exp(-28517/RT) T^{-1.5}$
R4	$r_{4a} = K_4 C_{\text{CH}_4} C_{\text{O}_2}$	$K_4 = 3.552 \times 10^{14} \exp(-130530/RT) T^{-1}$
R5	$r_{5a} = K_5 C_{\text{tar}} C_{\text{O}_2}$	$K_5 = 3.8 \times 10^7 \exp(-0.555 \times 10^8/RT)$
R6	$r_6 = \frac{6\epsilon_s \rho_s Y_c}{d_p \rho_s} \frac{1}{1/K_{6a} + 1/K_{6d}} C_{\text{O}_2}$	$K_{6a} = 596 \exp(-14965/RT) T_p$
R7	$r_7 = \frac{6\epsilon_s \rho_s Y_c}{d_p \rho_s} \frac{1}{1/K_{7a} + 1/K_{7d}} C_{\text{CO}_2}$	$K_{7a} = 2083 \exp(-149951/RT)$
R8	$r_8 = \frac{6\epsilon_s \rho_s Y_c}{d_p \rho_s} \frac{1}{1/K_{8a} + 1/K_{8d}} C_{\text{H}_2\text{O}}$	$K_{8a} = 63 \exp(-116820/RT)$
R9	$r_9 = K_9 C_{\text{HCN}} C_{\text{O}_2}$	$K_9 = 2.14 \times 10^8 \exp(-8.314 \times 10^7/RT)$
R10	$r_{10} = K_9 C_{\text{HCN}} C_{\text{O}_2} \frac{K_{10a}}{K_{10a} + K_{10b} C_{\text{NO}}}$	$K_{10b}/K_{10a} = 1.02 \times 10^{12} \exp(-2.12 \times 10^8/RT)$
R11	$r_{11} = K_9 C_{\text{HCN}} C_{\text{O}_2} \frac{K_{11b} C_{\text{NO}}}{K_{11a} + K_{11b} C_{\text{NO}}}$	$K_{11b}/K_{11a} = 1.02 \times 10^{12} \exp(-2.12 \times 10^8/RT)$
R12	$r_{12} = K_{12} C_{\text{N}_2\text{O}} C_{\text{CO}}$	$K_{12} = 1.24 \times 10^9 \exp(-4.9163 \times 10^7/RT)$
R13	$r_{13} = K_{13} C_{\text{N}_2\text{O}}$	$K_{13} = 1.5 \times 10^{11} \exp(-1.676 \times 10^8/RT)$
R14	$r_{14} = K_{14} C_{\text{NH}_3} C_{\text{O}_2}$	$K_{14} = 3.1 \times 10^8 \exp(-8.314 \times 10^7/RT)$
R15	$r_{15} = K_{15} C_{\text{NH}_3} C_{\text{O}_2}$	$K_{15} = 4.96 \times 10^8 \exp(-8.314 \times 10^7/RT)$
R16	$r_{16} = K_{16} \sqrt{C_{\text{NH}_3}} \sqrt{C_{\text{NO}}} \sqrt{C_{\text{O}_2}}$	$K_{16} = 1.1 \times 10^{15} \exp(-2.301 \times 10^8/RT)$
R17	$r_{17} = K_{17} \frac{K_{17a} C_{\text{NO}} (K_{17b} C_{\text{CO}} + K_{17c})}{K_{17a} C_{\text{NO}} + K_{17b} C_{\text{CO}} + K_{17c}}$	$K_{17} = 1.952 \times 10^7 \exp(-1.58 \times 10^8/RT)$ $K_{17a} = 18.26, \quad K_{17b} = 7.86, \quad K_{17c} = 0.002531$
R18	$r_{18} = \frac{6\epsilon_s \rho_s Y_c}{d_p \rho_s} K_{18} C_{\text{N}_2\text{O}}$	$K_{18} = 2.9 \times 10^9 \exp(-1.412 \times 10^8/RT)$
R19	$r_{19} = \frac{6\epsilon_s \rho_s Y_c}{d_p \rho_s} K_{19} C_{\text{NO}}$	$K_{19} = 5.85 \times 10^7 \exp(-9.977 \times 10^7/RT)$
R20	$r_{20} = \frac{6\epsilon_s \rho_s Y_c}{d_p \rho_s} K_{20} C_{\text{NO}}$	$K_{20} = 1.3 \times 10^5 \exp(-1.423 \times 10^7/RT)$
R21	$r_{21} = \frac{\epsilon_s \rho_s Y_{\text{CaO}}}{\rho_{\text{CaO}}} \eta K_{21} C_{\text{SO}_2}$	$K_{21} = 1.1 \times 10^6 \exp(-0.595 \times 10^8/RT)$ $\eta = \exp(-5.71X)$ $X = C_{\text{CaSO}_4}/(C_{\text{CaO}} + C_{\text{CaSO}_4})$

where C_{e1} and C_{e2} are the constants and σ_k and σ_e are the turbulent Prandtl numbers.

The momentum equation of the solid phase is

$$\frac{\partial(\alpha_s \rho_s)}{\partial t} + \nabla(\alpha_s \rho_s v_s) = -\alpha_s \nabla p + \alpha_s \rho_s g - \beta(v_s - v_g) + \nabla(\alpha_s \tau_s) + S_{sg} v_s \quad (15)$$

where τ_s is the solid-phase stress tensor and p_s is the solid pressure. They are expressed as

$$\tau_s = \left[(-p_s + \lambda_s \nabla v_s) + \mu_s [\nabla v_s + (\nabla v_s)^T] - \frac{2}{3} (\nabla v_s) \right] I \quad (16)$$

$$\lambda_s = \frac{4}{3} \alpha_s \rho_s d_{s0} (1 + e) \sqrt{\frac{\Theta_s}{\pi}} \quad (17)$$

$$\mu_s = \frac{4}{5} \alpha_s^2 \rho_s d_{s0} (1 + e) \sqrt{\frac{\Theta_s}{\pi}} + \frac{10 \rho_s d_s \sqrt{\pi \Theta_s}}{96(1 + e) \alpha_{s0}} \left[1 + \frac{4}{5} \alpha_{s0} (1 + e) \right]^2 + \frac{p_s \sin \varphi}{2 \sqrt{I_{2D}}} \quad (18)$$

$$p_s = \alpha_s \rho_s \Theta [1 + 2g_0 \alpha_s (1 + e)] \quad (19)$$

$$g_0 = \left[1 - \left(\frac{\alpha_s}{\alpha_{s,\max}} \right)^{1/3} \right]^{-1} \quad (20)$$

$$\frac{3}{2} \left[\frac{\partial}{\partial t} (\alpha_s \rho_s \Theta_s) + \nabla(\alpha_s \rho_s \Theta_s v_s) \right] = -(p_s I + \tau_s) : \nabla v_s + \nabla(k_s \nabla \Theta_s) - \gamma - 3\beta \Theta_s \quad (21)$$

$$k_s = \frac{150\rho_s d_s \sqrt{\Theta_s \pi}}{384(1 - \epsilon)g_0} \left[1 + \frac{6}{5} \alpha_{sg_0} (1 + \epsilon) \right]^2 + 2\rho_s \alpha_s^2 d_{sg_0} (1 + \epsilon) \sqrt{\frac{\Theta_s}{\pi}} \quad (22)$$

$$\gamma = 3(1 - \epsilon^2) \alpha_s^2 \rho_s \Theta_s \left(\frac{4}{d_s} \sqrt{\frac{\Theta}{\pi}} - \nabla v_s \right) \quad (23)$$

To describe the conservation of energy in Eulerian–Eulerian models, a separate enthalpy equation is used for each phase. Heat transfer within each phase and heat exchange between the gas and solid phases are considered, but the viscous heating is neglected.

$$\frac{\partial}{\partial t} (\alpha_g \rho_g H_g) + \nabla (\alpha_g \rho_g v_g H_g) = \nabla (\lambda_g \nabla T_g) + h_{gs} (T_g - T_s) + S_{gs} H_s \quad (24)$$

$$\frac{\partial}{\partial t} (\alpha_s \rho_s H_s) + \nabla (\alpha_s \rho_s v_s H_s) = \nabla (\lambda_s \nabla T_s) + h_{sg} (T_s - T_g) + S_{sg} H_s \quad (25)$$

where H , λ , h are the specific enthalpy, the mixture thermal conductivity, and the heat-transfer coefficient between the gas and solid phases, respectively. The $S_{gs} H_s$ is the heat source from chemical reactions. The heat-transfer coefficient is expressed as

$$h_{gs} = h_{sg} = \frac{6\lambda_g \alpha_g \alpha_s Nu_s}{d_s^2} \quad (26)$$

The Nusselt number correlation proposed by Gunn is used in the present model

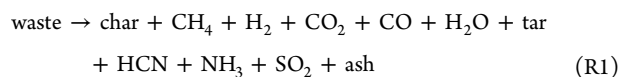
$$Nu_s = (7 - 10\alpha_g + 5\alpha_g^2)(1 + 0.7Re_s^{0.2}Pr^{1/3}) + (1.33 - 2.4\alpha_g + 1.2\alpha_g^2)Re_s^{0.7}Pr^{1/3} \quad (27)$$

where Pr is the continuous-phase Prandtl number.

2.2. Chemical Reactions. The combustion process of solid waste consists of waste devolatilization, volatile (CO , H_2 , CH_4 , and tar) combustion, char combustion and gasification, and pollutant (NO , N_2O , and SO_2) emissions. It is assumed that the solid phase includes six components: dry waste ($\text{C}_{4.316}\text{H}_{6.718}\text{O}_{2.538}\text{N}_{0.054}\text{S}_{0.00415}$), char ($\text{CN}_{0.0065}\text{S}_{0.0005}$), calcium oxide (CaO), calcium sulfate (CaSO_4), ash, and sand. The gas phase includes 14 components: oxygen (O_2), nitrogen (N_2), carbon dioxide (CO_2), water vapor (H_2O), carbon monoxide (CO), hydrogen (H_2), methane (CH_4), tar ($\text{CH}_{5.7}\text{O}_{0.071}$), hydrogen cyanide (HCN), ammonia (NH_3), sulfur dioxide (SO_2), cyanotic (CNO), nitric oxide (NO), and nitrous oxide (N_2O).

2.2.1. Devolatilization. During the devolatilization process, the waste volatile components are released on entry into the reactor. The composition balance is considered as follows: (1) The gas products of devolatilization are CO_2 , CO , H_2O , H_2 , CH_4 , HCN , NH_3 , SO_2 , and tar. (2) The contents of CO_2 , CO , H_2O , H_2 , and CH_4 are estimated from the results of pyrolysis tests.²² (3) The equivalent formulas and amounts of dry waste, char, and tar are derived from the proximate and ultimate analyses of the fuel, which are shown in Table 1.

The devolatilization of solid waste can be expressed as



The single-step model is used to describe the reaction rate of the devolatilization reaction in the present work²³

$$\frac{dV_t}{dt} = A \exp\left(\frac{-E}{RT}\right) (V_0 - V_t) \quad (28)$$

where V_t and V_0 are the instantaneous and total amounts of volatile matter, respectively. The parameters in this model are selected as $A = 1.43 \times 10^3 \text{ s}^{-1}$ and $E = 8.86 \times 10^7 \text{ J/kmol}$.

2.2.2. Volatile Combustion. The finite-rate/Eddy-dissipation model is used to calculate the homogeneous reaction rate, which computes both the Arrhenius rate and the mixing rate and uses the smaller of the two.²⁰

$$r_c = \min(r_a, r_e) \quad (29)$$

$$r_a = k_a T^z C_A^n C_B^m \quad (30)$$

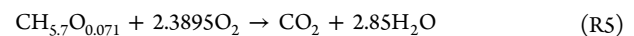
$$r_e = \gamma_{c,i} M_{w,i} B_i \rho \frac{\epsilon}{k} \min\left(\min\left(\frac{Y_R}{\gamma_{c,R} M_{w,R}}\right), B_2 \frac{\sum_P Y_P}{\sum_j \gamma_{c,j} M_{w,j}}\right) \quad (31)$$

where C is the mole concentration of the reactant and n and m are rate exponents. k is the rate coefficient with Arrhenius formula

$$k = AT^n \exp\left(\frac{-E}{RT}\right) \quad (32)$$

where A is the pre-exponential constant, E is the activation energy, and R is the universal gas constant.

The combustion process of volatile components considers the following four reactions:



2.2.3. Char Combustion. In this study, the “shrinking core” model is used to describe the reactions between char and gas. It is assumed that the reaction rate is controlled by both the kinetics of char combustion and the diffusion of gas species through the gas boundary layer.

The char reaction rate is expressed as

$$r_c = \frac{6V_c}{d_s} [(K_a)^{-1} + (K_d)^{-1}]^{-1} p_i \quad (33)$$

where V_c is the char volume and p_i is the pressure of the i th gas species. K_a is the kinetic rate constant, which is calculated from the Arrhenius equation. K_d is the diffusion rate coefficient

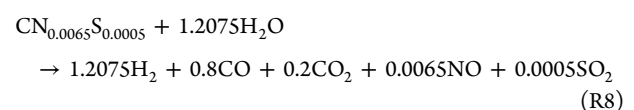
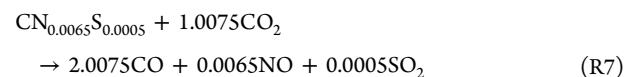
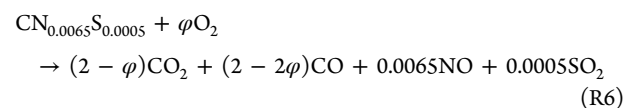
$$K_d = \frac{Sh D_{gs} M_{w,c}}{RT_s d_s} \quad (34)$$

where Sh and D_{gs} are the Sherwood number and diffusion coefficient, respectively.

$$Sh = 2 + 0.654Re^{1/2}Pr^{1/3} \quad (35)$$

$$D_{gs} = 8.34 \times 10^{-6} T^{1.75} p^{-1} \quad (36)$$

The heterogeneous reactions of char combustion and char gasification are written as



where the distribution coefficient in eq R6 is given by²⁴

$$\phi = \frac{2 + \chi}{2 + 2\chi} \quad (37)$$

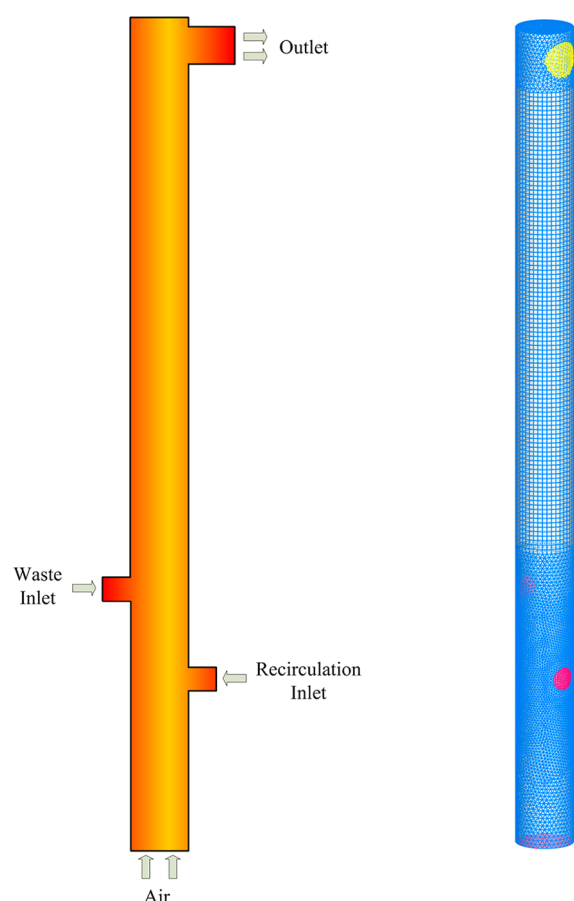


Figure 2. Sketch of the CFB riser and numerical grid.

Table 3. Modeling Conditions

run	1	2	3
fuel feed rate, Q_m (kg h^{-1})	15.0	15.5	15.5
mass flux of solid circulation, G_s ($\text{kg m}^{-2} \text{s}^{-1}$)	9.0	9.5	9.4
superficial velocity at room temperature, U_0 (m s^{-1})	1.75	2.11	2.24
bed temperature, T_{bed} ($^{\circ}\text{C}$)	860	807	839
excess air ratio, EA	1.10	1.21	1.28

$$\chi = 2500 \exp\left(-\frac{6240}{T}\right) \quad (38)$$

2.2.4. Nitrogen Oxide Emission. During the devolatilization, nitrogen and sulfur contained in the waste are partially released as volatile and partially retained in the solid char. In this paper, the volatile N concentration partitioned is identical to that in the dry, ash-free waste.¹⁸ The main reaction routes of fuel nitrogen to NO, N_2O , and N_2 during combustion are summarized in Figure 1.² Char N is emitted as NO through the char combustion and gasification reactions R6–R8. The primary intermediates NH_3 and HCN will preferentially be formed from volatiles. The ratio of HN_3/HCN depends upon the fuel and experimental conditions. HCN can convert into CNO quickly, which is an intermediate product and further reacts with O_2 to give NO or give N_2O with NO. NH_3 reacts with O_2 directly under sufficient O_2 conditions, which can convert into NO or N_2 . The concentration of char in the reactor is important, because NO and N_2O can be reduced to N_2 by char.²⁵ The detailed reactions for nitrogen oxide emission are described as follows:

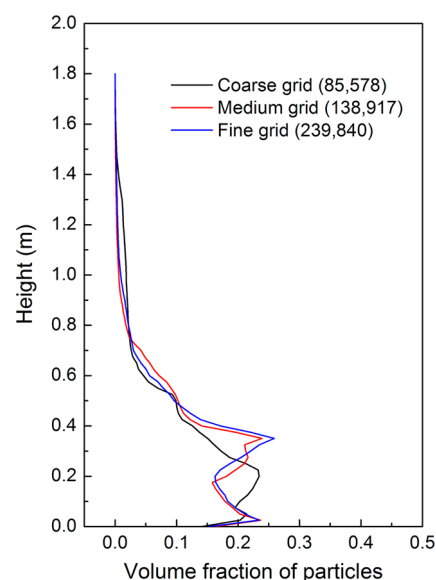
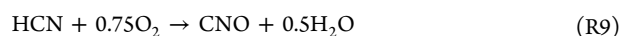


Figure 3. Profiles of solid concentrations with different grid sizes.

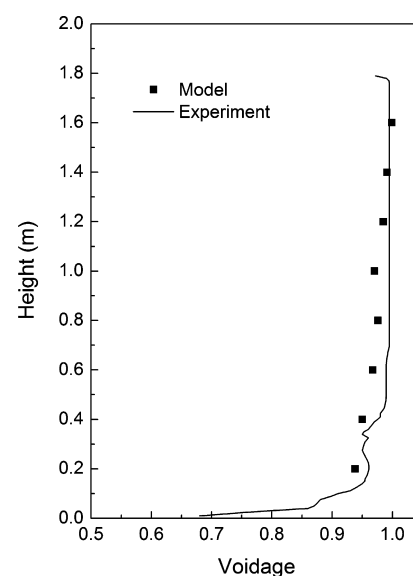
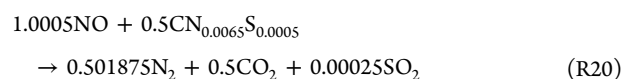
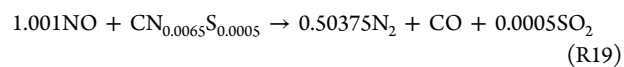
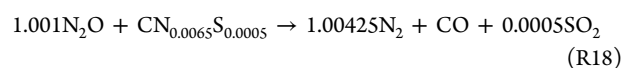
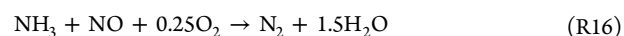
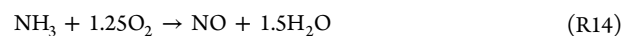


Figure 4. Comparison of voidage distributions.



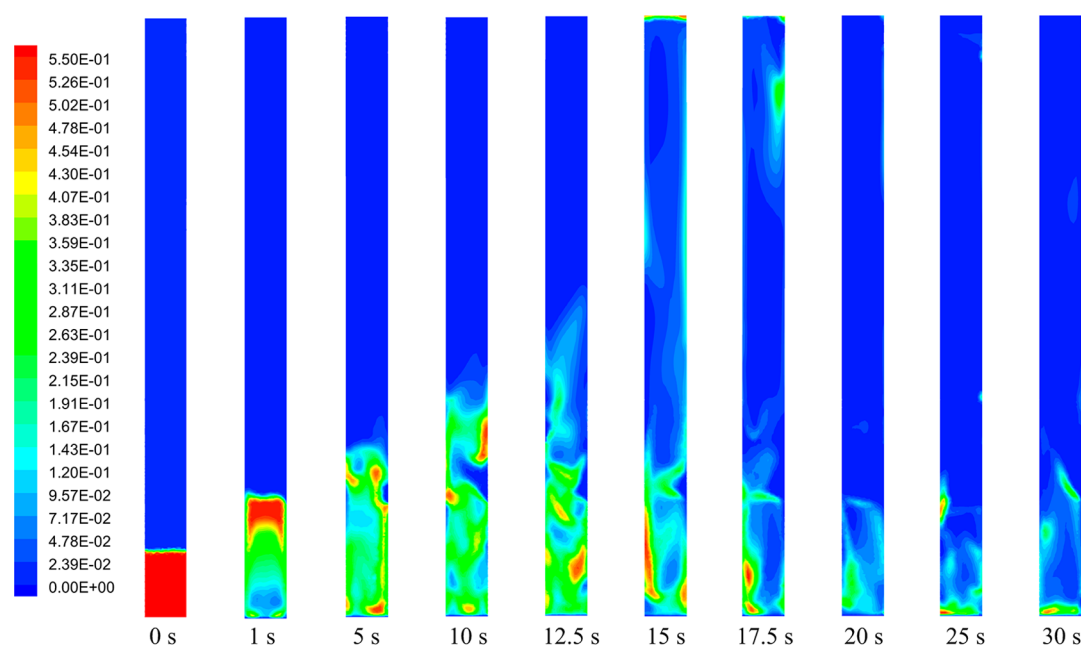


Figure 5. Flow pattern transformation with time colored with the solid volume fraction.

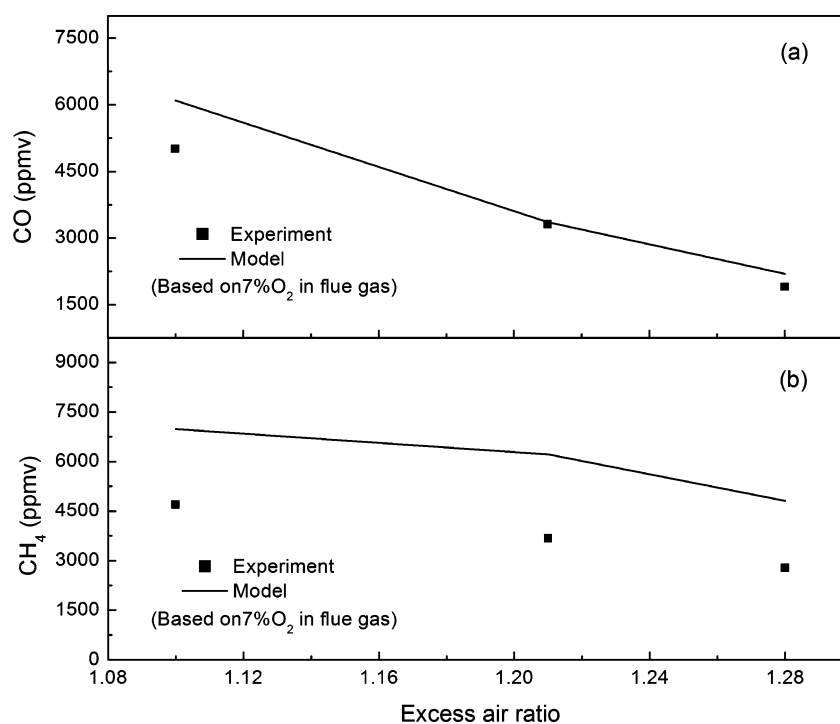
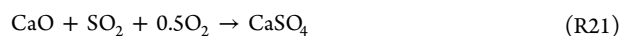


Figure 6. Effect of EA on CO and CH₄ emissions.

2.2.5. Sulfur Dioxide Emission. As mentioned above, the volatile S is released as acid gas SO₂ during waste devolatilization. Char S can also convert to SO₂ through the char oxidation and reduction reactions R6–R8 and R18–R20, respectively. The combustion desulfurization method by means of the desulfurizing agent during the combustion process is widely used. The main component of the desulfurizing agent is currently calcium carbonate.¹⁹ The ash composition of waste contains calcium oxide, CaO, which can also absorb a part of the sulfur dioxide as calcium sulfate. The sulfation reaction between CaO and SO₂ is expressed as



The rate expressions and kinetic parameters for volatile combustion reactions, char combustion and gasification reactions, nitrogen

and sulfur emission reactions are taken from Destroches-Ducarne et al.,³ Zhou et al.,¹⁸ and Wang et al.²⁰ and are summarized in Table 2.

2.3. Computational Geometry and Model Setup. The developed Eulerian–Eulerian model is applied to the simulation of a CFB combustor conducted by Topal et al.²⁶ The riser is a fully cylindrical column with a diameter of 0.125 m and a height of 1.8 m, which is connected to the cyclone at the top by an 80 mm diameter pipe. Figure 2a shows the sketch of the CFB riser. The solid recirculating inlet is located at a level of 370 mm above the distributor plate. The air split ratio between recirculation and the primary air is 1:5. Olive cake (OC), a waste of olive oil mill, is used as fuel. Silica sand and ash are used as bed materials. The average particle sizes are

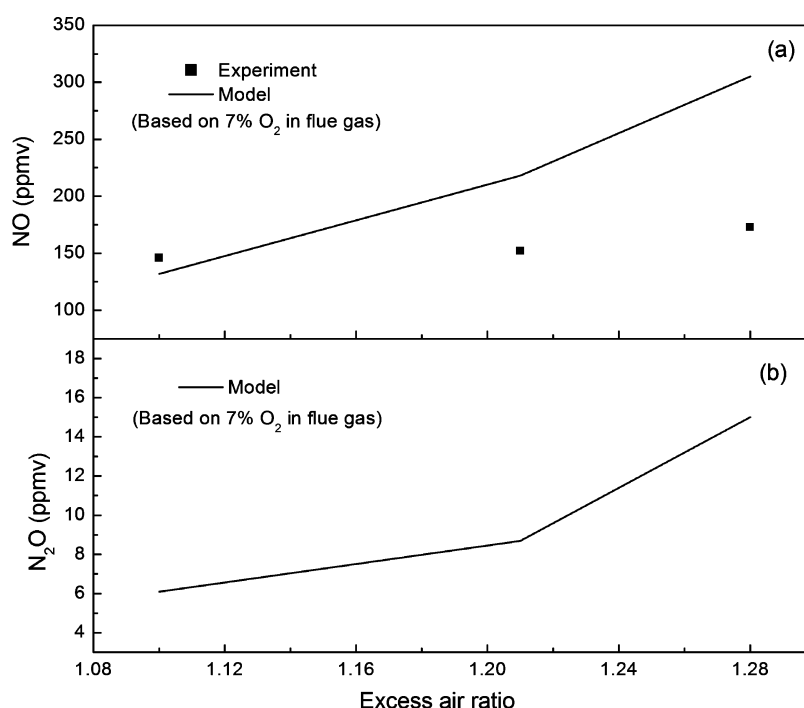


Figure 7. Effect of EA on NO and N₂O emissions.

2.30 and 0.56 mm for OC and sand particles, respectively. The amount of combustibles from the recirculating ash is found to be between 7 and 10 wt %. The contents of CaO in the ash are deduced from the ash component analysis in Table 1.

The silica sand is used as bed material with the initial bed height of 0.2 m, which has the volume fraction of 0.55. The packing limit is also set as 0.55. At the air, fuel feeding, and recirculation inlets, velocities of gas and solid are specified. At the outlet, the outflow boundary condition is adopted. At the walls, the no-slip condition is set and the heat flux is zero. At first, air–sand fluidization is simulated without fuel feeding. After the basic flow pattern is reached, the solid waste is fed into the CFB riser. Detailed modeling conditions are given in Table 3.

The Eulerian–Eulerian model is established and computed on the basis of FLUENT software. All mathematical models described above are solved using a finite volume method. The first-order upwind discretization scheme is used for all convective terms. Because the gas–solid flow is coupled with chemical reactions, the computation is complex and time-consuming. Although less accurate, the first-order scheme will ensure that the solution is more robust and converges faster.^{20,27} The Green–Gauss cell-based method is applied to calculate the gradients of the variables, and the algorithm of phase coupled SIMPLE is chosen for pressure–velocity coupling. The heterogeneous reaction rates are added through the user-defined function. The constant time step is set as 1×10^{-4} s.

Figure 2b shows the numerical grid used in the riser field. The middle section of the riser is divided with the hexahedral/wedge mesh elements, and the bottom and top regions are divided with tetrahedral mesh elements. For the fuel feeding inlet and recirculation inlet, local mesh refinements are adopted. To obtain the results of the mesh sensitivity analysis, three different grids are tested, containing 85 578, 138 917, and 239 840 grid cells. The concentration profiles of particles along the height of the CFB riser without fuel feeding are illustrated in Figure 3. The results reveal that the fine grid and medium grid predict similar profiles of particle concentrations, while the result of the coarse grid has obvious differences. In view of the influences of computation time and calculation accuracy, the medium grid size is chosen in the following work.

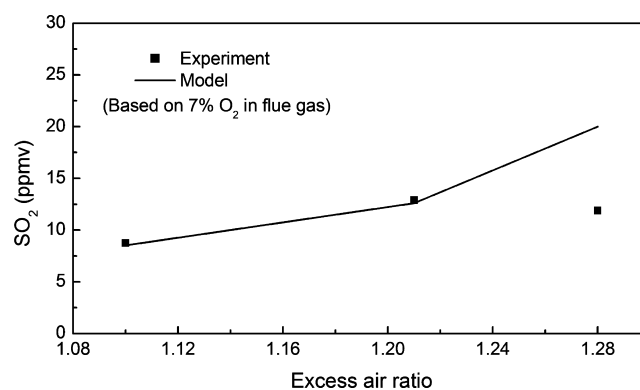


Figure 8. Effect of EA on SO₂ emissions.

3. RESULTS AND DISCUSSION

3.1. Flow Characteristics. The model is employed to study the hydrodynamic of the CFB riser before the gaseous emission research. Figure 4 shows the comparison of axial distribution of voidage between the simulations and experiments in the hot CFB. Predicted results are drawn from the time-averaged value. As shown in Figure 4, the simulation results generally agree well with the experimental data. The dilute region in the upper section of the riser and the dense region in the bottom section are presented by the model. The voidage gradually increases along the height of the riser but suddenly decreases at the top, which indicates that the outlet geometry results in a gathering of particles in this region.²⁸ Because of the unrealistic setup of the average size of the particles, a small distinction between the simulations and measurements cannot be avoided.

A full development of the flow patterns in the CFB riser is illustrated with solid volume fraction in Figure 5. It can be seen that the particles gradually move up with time and the voidage of the bottom region increases. When parts of suspended particles reach the top of the riser, they are carried over to the cyclone. Meanwhile, the recycled particles are reintroduced into the bed to

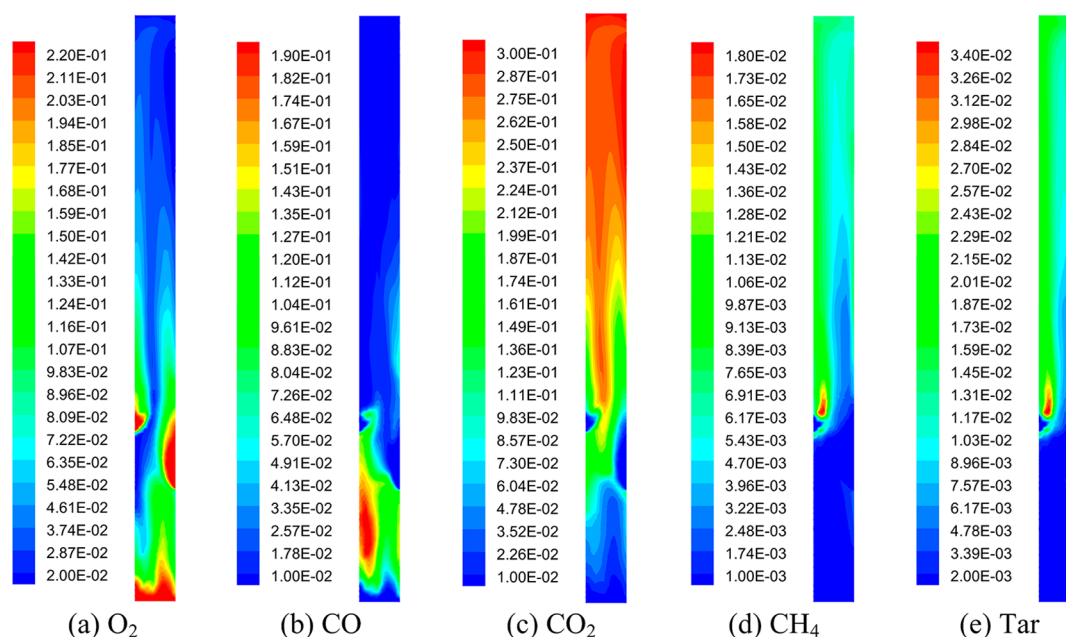


Figure 9. Mass fraction profiles of main combustion gases (EA, 1.10; Q_f , 15.0; G_s , 9.0; U_0 , 1.75; and T_{bed} , 860).

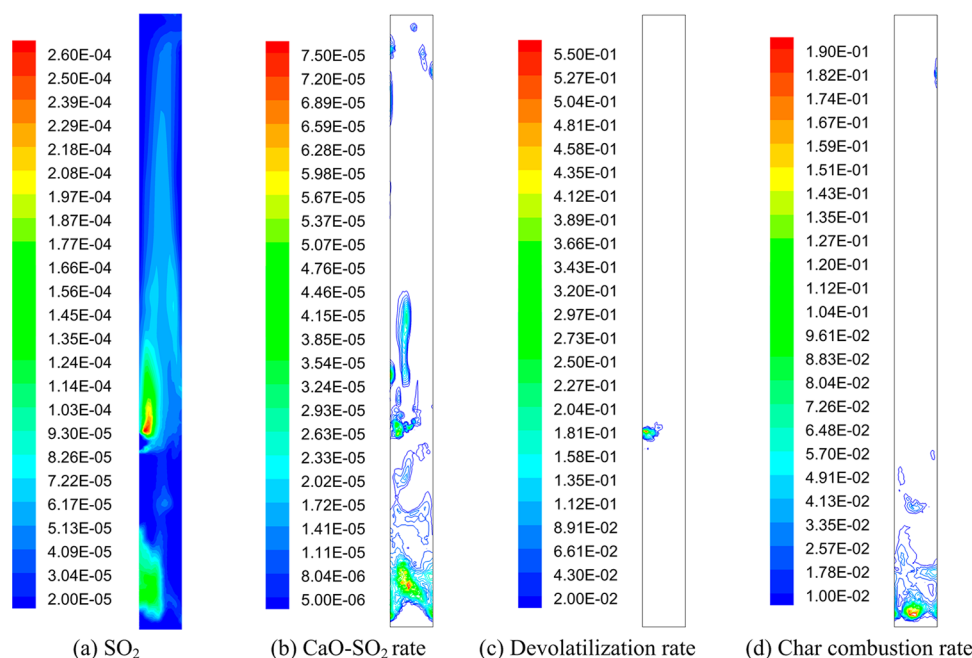


Figure 10. Mass fraction profiles of the SO_2 concentration and related reaction rates (EA, 1.10; Q_f , 15.0; G_s , 9.0; U_0 , 1.75; and T_{bed} , 860).

maintain the steady bed inventory. A typical turbulent fluidization takes on at the lower section of the riser. Some particle clusters close to the wall can also be observed from Figure 5.

3.2. Gas Emissions. Figure 6 shows the variation of CO and CH_4 emissions with EA predicted by the model in comparison to experimental data. Detailed modeling conditions for three cases are given in Table 3. To eliminate the air dilution effect, the emissions are based on 7% O_2 in the flue gas. As shown in Figure 6, the CO and CH_4 concentrations gradually decrease with the increasing excess air ratio. This means that the volatiles released from the fuel and char particles burn more completely when the excess air increases. The profile of experimental data shows the same tendency.

Figure 7 illustrates the effect of EA on NO and N_2O emissions, which are based on 7% O_2 in the flue gas. From Figure 7a, it can be observed that the predicted NO concentration increases with the increasing EA. In the CFB combustor, NO is formed through the oxidation of HCN and NH_3 released from devolatilization and combustion of nitrogen retained in the char. When the total excess air increases, the NO formation reactions are strengthened. On the other hand, NO reduction is unfavored because of the lower CO and NH_3 contents and the reduced amounts of char in the riser. The two reasons result in a growth in NO emission. The comparison between simulations and experiments shows that the model correctly predicts the variation trend of the NO emission. Under high excess air, the increment of the NO concentration intensifies N_2O

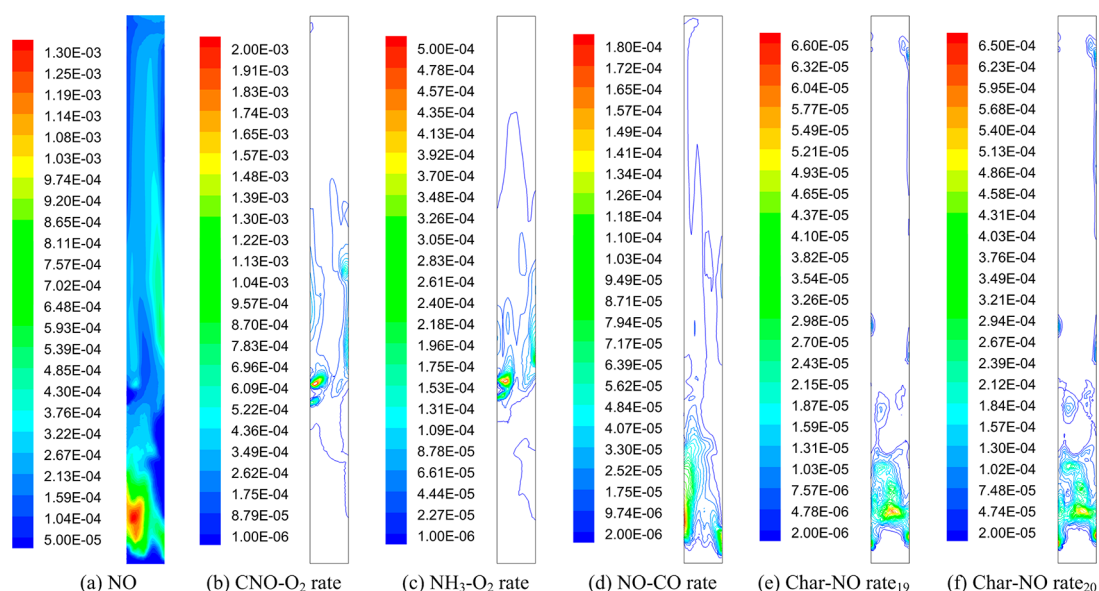


Figure 11. Mass fraction profiles of the NO concentration and related reaction rates (EA, 1.10; Q_b , 15.0; G_s , 9.0; U_0 , 1.75; and T_{bed} , 860).

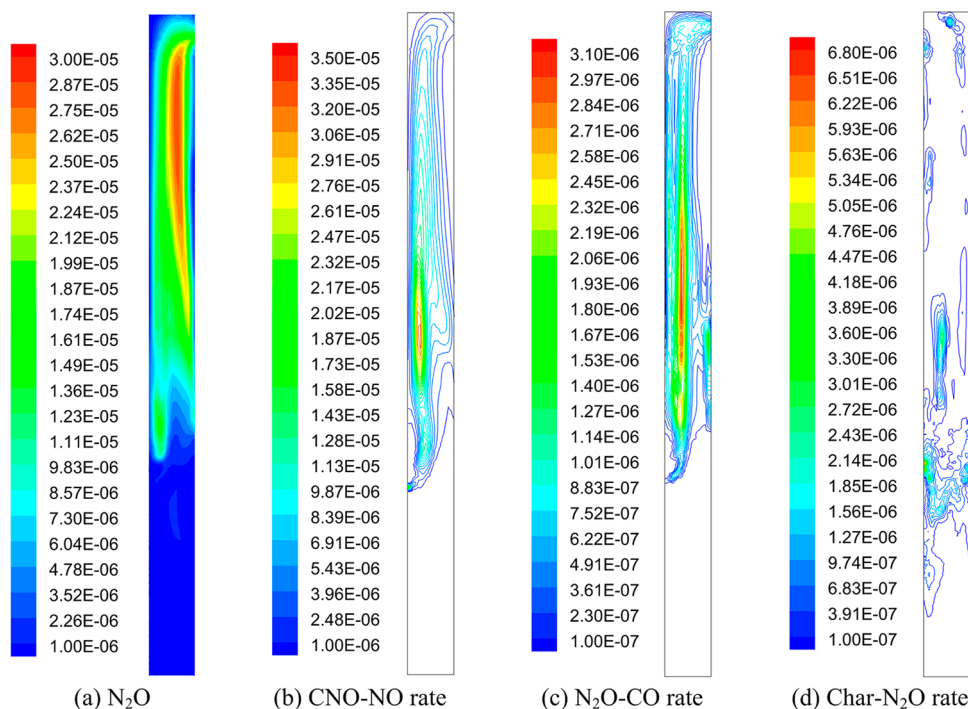


Figure 12. Mass fraction profiles of the N_2O concentration and related reaction rates (EA, 1.10; Q_b , 15.0; G_s , 9.0; U_0 , 1.75; and T_{bed} , 860).

formation through the reaction between NO and CNO. Moreover, N_2O reduction by char and CO is weakened. Hence, the emission of N_2O shows an increase with the increase of excess air in Figure 7b.

The SO_2 emission based on 7% O_2 in the flue gas is plotted with the EA in Figure 8. It can be seen that emission of SO_2 gradually increases when excess air increases. More air introduced into the riser not only enhances char combustion but also causes more SO_2 to be recaptured by CaO. Therefore, there is an uncertainty on SO_2 emission. The experimental results show that the SO_2 emission first increases and then slightly decreases. The deviation between simulations and experiments may be related to the SO_2 capture rate, which is of various expressions in the literature.¹⁸

3.3. Distributions of Gas Compositions. The concentration distributions of the major combustion gases in the riser are shown in Figure 9. The form of time-averaged mass fraction is adopted for all simulation results. Because air is introduced to the bed by entrainment of fuel particles and recirculating solid as well as supplied from the bottom, the mass fraction of O_2 is higher near the primary air inlet, recirculating inlet, and fuel inlet. Then, the O_2 concentration gradually decreases along the riser height because of the volatiles and char combustions. Consequently, the CO_2 concentration profile shows the contrary tendency. Because of the devolatilization, a certain concentration of CO takes on close to the fuel inlet. The peak concentration of CO appears in the lower region, which is attributed to char combustion. Because CH_4 and tar are

produced through devolatilization, large amounts of CH_4 and tar are present near the fuel feeding point.

Figure 10 illustrates the mass fraction distributions of the SO_2 concentration and related reaction rates. In panels c and d of Figure 10, the high devolatilization rate exists in a tiny zone close to the fuel feeding point and the char combustion reaction occurs at the lower part of the riser. SO_2 is mainly formed by these two reactions. Consequently, the mass fraction of SO_2 is high near the fuel inlet and in the bottom region (Figure 10a). The distributions of sulfation reaction rates between CaO and SO_2 are shown in Figure 10b. CaO is from the ash contained in the OC, and more particles gather in the dense phase zone and near the fuel feeding inlet, where the higher SO_2 capture rates are located.

The mass fraction profiles of the NO concentration and related reaction rates are displayed in Figure 11. It can be seen from panels a–c of Figure 11 that the high concentration of NO is located at the lower section of the riser and near the fuel inlet, where the heterogeneous char combustion and homogeneous oxidation reactions take place. The NH_3 oxidation rate is 1 magnitude smaller than the CNO oxidation rate. Panels d–f of Figure 11 show the NO reduction reaction rates, which include two heterogeneous reactions between char and NO and one homogeneous reaction between CO and NO. The char–NO reactions mainly occur at the bottom of the riser because of the existence of solid char, while the NO–CO reaction occurs in a slightly larger range. The three reactions have a similar rate magnitude, indicating the equal significance to the reduction of NO.

Figure 12 illustrates the mass fraction profiles of the N_2O concentration and related reaction rates. As seen in panels a and b of Figure 12, the high value of the mass fraction appears at the upper part of the riser because the N_2O formation reaction between CNO and NO takes place above the fuel feeding point. Panels c and d of Figure 12 show the N_2O reduction reactions by CO and char, respectively. The N_2O –CO reaction occurs in the upper region, while the N_2O –char reaction occurs near the fuel inlet. The two reaction rates are in the same order of magnitude.

4. CONCLUSION

A 3D numerical model has been developed to predict the gaseous pollutant emissions during the combustion of solid waste in a CFB combustor. On the basis of the Eulerian–Eulerian approach, the gas phase is modeled with the k – ϵ turbulence model and the particle phase is modeled with the kinetic theory of granular flow. Reactions during combustion consist of waste devolatilization, volatile combustion, char combustion, SO_2 formation and recapture by calcium oxide, NO and N_2O formation, and diminution by heterogeneous and homogeneous reactions.

The model has been applied to the CFB riser with a height of 1.8 m and a diameter of 0.125 m at atmosphere. Simulation obtains the hydrodynamic characteristics in the riser, including the axial distribution of bed voidage and the flow pattern transformation with time. The modeling focuses mostly on the gaseous pollutant emission, profiles of gas compositions, and related reaction rates in the riser. Increasing EA results in a sharp decrease in the emissions of CO and CH_4 . The predicted emissions of NO and N_2O gradually increase with the increasing excess air. The SO_2 emission also presents a growth when excess air increases. The mass fraction of SO_2 is high near the fuel inlet and in the bottom region, where the devolatilization and char combustion take place. The higher

SO_2 capture rates are also located in the two regions. The NO concentration profile is similar to that of SO_2 , while the NO reduction reactions mainly occur in the lower region of the riser because of the existence of solid char and CO. The high concentration of N_2O just appears above the fuel inlet as a result of devolatilization.

AUTHOR INFORMATION

Corresponding Author

*Telephone: +86-25-83794744. Fax: +86-25-83795508. E-mail: wqzhong@seu.edu.cn.

Notes

The authors declare no competing financial interest.

ACKNOWLEDGMENTS

Financial support from the Major Program of the National Natural Science Foundation of China (51390492), the National Science Fund for Distinguished Young Scholars of China (51325601), the Major State Basic Research Development Program of China (2011CB201505), and the U.K. Engineering and Physical Sciences Research Council (EPSRC/China Project EP/G063176/1) is sincerely acknowledged.

NOMENCLATURE

- C_d = drag coefficient
- d_s = particle diameter (mm)
- D_{gs} = diffusion coefficient for gas ($\text{m}^2 \text{s}^{-1}$)
- g_0 = radial distribution function
- G_s = mass flux of solid circulation ($\text{kg m}^{-2} \text{s}^{-1}$)
- h = heat-transfer coefficient ($\text{W m}^{-2} \text{K}^{-1}$)
- H = specific enthalpy (J kg^{-1})
- J_i = diffusion flux ($\text{kg m}^{-2} \text{s}^{-1}$)
- k = turbulent kinetic energy ($\text{m}^2 \text{s}^{-2}$)
- K = reaction rate constant
- K_a = kinetic rate constant
- K_d = diffusion rate coefficient
- M_w = molecular weight (kg kmol^{-1})
- Nu = Nusselt number
- p = pressure (Pa)
- Pr = Prandtl number
- Q_f = fuel feed rate (kg h^{-1})
- r = reaction rate ($\text{kmol m}^{-3} \text{s}^{-1}$)
- R = universal gas constant ($\text{J kmol}^{-1} \text{K}^{-1}$)
- Re = Reynolds number
- S = mass source term
- Sc_t = Schmidt number
- Sh = interphase energy exchange rate
- T = temperature (K)
- U_0 = superficial velocity at room temperature (m s^{-1})
- V = volume (m^3)
- Y_i = mass fraction

Greek Letters

- α = volume fraction
- β = gas–solid interphase drag coefficient
- γ = dissipation of fluctuating energy (W m^{-3})
- ϵ = dissipation rate of turbulent kinetic energy ($\text{m}^2 \text{s}^{-3}$)
- λ = thermal conductivity ($\text{W m}^{-2} \text{K}^{-1}$)
- μ = viscosity ($\text{kg m}^{-1} \text{s}^{-1}$)
- v = mean velocity (m s^{-1})
- ν = instantaneous velocity (m s^{-1})
- ρ = density (kg m^{-3})
- τ = stress tensor (Pa)

Subscripts

- g = gas phase
i = ith species
l = laminar flow
s = solid phase
t = turbulent flow

■ REFERENCES

- (1) de Diego, L. F.; de las Obras-Loscertales, M.; Rufas, A.; García-Labiano, F.; Gayán, P.; Abad, A.; Adánez, J. *Appl. Energy* **2013**, *102*, 860–867.
- (2) Van Caneghem, J.; Brems, A.; Lievens, P.; Block, C.; Billen, P.; Vermeulen, I.; Dewil, R.; Baeyens, J.; Vandecasteele, C. *Prog. Energy Combust.* **2012**, *38*, 551–582.
- (3) Desroches-Ducarne, E.; Dolignier, J. C.; Marty, E.; Martin, G.; Delfosse, L. *Fuel* **1998**, *77*, 1399–1410.
- (4) Gómez-Barea, A.; Leckner, B. *Prog. Energy Combust.* **2010**, *36*, 444–509.
- (5) Chen, Z.; Lin, M.; Ignowski, J.; Kelly, B.; Linjewile, T. M.; Agarwal, P. K. *Fuel* **2001**, *80*, 1259–1272.
- (6) Gungor, A. *Chem. Eng. J.* **2009**, *146*, 388–400.
- (7) Krzywanski, J.; Rajczyk, R.; Bednarek, M.; Wesolowska, M.; Nowak, W. *Fuel Process. Technol.* **2013**, *116*, 27–34.
- (8) Myohanen, K.; Hyppanen, T. *Int. J. Chem. React. Eng.* **2011**, *9*.
- (9) Gungor, A. *Fuel* **2008**, *87*, 1453–1468.
- (10) Yang, X.; Liu, B.; Song, W.; Lin, W. *Energy Fuels* **2011**, *25*, 3718–3730.
- (11) Jia, L.; Tan, Y.; Anthony, E. J. *Energy Fuels* **2010**, *24*, 910–915.
- (12) Liu, H.; Gibbs, B. M. *Fuel* **2002**, *81*, 271–280.
- (13) Oevermann, M.; Gerber, S.; Behrendt, F. *Particuology* **2009**, *7*, 307–316.
- (14) Wischniewski, R.; Ratschow, L.; Hartge, E.-U.; Werther, J. *Particuology* **2010**, *8*, 67–77.
- (15) Rong, D.; Horio, M. DEM simulation of char combustion in a fluidized bed. *Proceedings of the 2nd International Conference on CFD in the Minerals and Process Industries*; Melbourne, Victoria, Australia, Dec 6–8, 1999; pp 65–70.
- (16) Yunhau, Z.; Huilin, L.; Yurong, H.; Ding, J.; Lijie, Y. *Chem. Eng. J.* **2006**, *118*, 1–10.
- (17) Shuyan, W.; Lijie, Y.; Huilin, L.; Ding, J.; Yu, L.; Xiang, L. *Fuel* **2008**, *87*, 870–877.
- (18) Zhou, W.; Zhao, C. S.; Duan, L. B.; Chen, X. P.; Liang, C. *Chem. Eng. J.* **2011**, *173*, 564–573.
- (19) Yu, G.; Chen, J.; Li, J.; Hu, T.; Wang, S.; Lu, H. *Energy Fuels* **2014**, *28*, 2227–2235.
- (20) Wang, X. F.; Jin, B. S.; Zhong, W. Q. *Chem. Eng. Process.* **2009**, *48*, 695–705.
- (21) Yu, L.; Lu, J.; Zhang, X. P.; Zhang, S. J. *Fuel* **2007**, *86*, 722–734.
- (22) Syamlal, M.; O'Brien, T. *AIChE Symp. Ser.* **1989**, *85*, 22–31.
- (23) Radmanesh, R.; Chaouki, J.; Guy, C. *AIChE J.* **2006**, *52*, 4258–4272.
- (24) de Souza-Santos, M. L. *Solid Fuels Combustion and Gasification: Modeling, Simulation, and Equipment Operations*; CRC Press: Boca Raton, FL, 2004.
- (25) Winter, F.; Wartha, C.; Hofbauer, H. *Bioresour. Technol.* **1999**, *70*, 39–49.
- (26) Topal, H. *Fuel* **2003**, *82*, 1049–1056.
- (27) Benyahia, S.; Arastoopour, H.; Knowlton, T. M. *Chem. Eng. Commun.* **2002**, *189*, 510–527.
- (28) Zhou, W.; Zhao, C. S.; Duan, L. B.; Qu, C. R.; Chen, X. P. *Chem. Eng. J.* **2011**, *166*, 306–314.